



Material classification from sparse spectral X-ray CT using vectorial total variation based on L infinity norm

Jumanazarov, Doniyor; Koo, Jakeoung; Kehres, Jan; Poulsen, Henning F.; Olsen, Ulrik L.; Iovea, Mihai

Published in:
Materials Characterization

Link to article, DOI:
[10.1016/j.matchar.2022.111864](https://doi.org/10.1016/j.matchar.2022.111864)

Publication date:
2022

Document Version
Publisher's PDF, also known as Version of record

[Link back to DTU Orbit](#)

Citation (APA):
Jumanazarov, D., Koo, J., Kehres, J., Poulsen, H. F., Olsen, U. L., & Iovea, M. (2022). Material classification from sparse spectral X-ray CT using vectorial total variation based on L infinity norm. *Materials Characterization*, 187, Article 111864. <https://doi.org/10.1016/j.matchar.2022.111864>

General rights

Copyright and moral rights for the publications made accessible in the public portal are retained by the authors and/or other copyright owners and it is a condition of accessing publications that users recognise and abide by the legal requirements associated with these rights.

- Users may download and print one copy of any publication from the public portal for the purpose of private study or research.
- You may not further distribute the material or use it for any profit-making activity or commercial gain
- You may freely distribute the URL identifying the publication in the public portal

If you believe that this document breaches copyright please contact us providing details, and we will remove access to the work immediately and investigate your claim.



Material classification from sparse spectral X-ray CT using vectorial total variation based on L infinity norm

Doniyor Jumanazarov ^{a,c,*}, Jakeoung Koo ^b, Jan Kehres ^a, Henning F. Poulsen ^a, Ulrik L. Olsen ^a, Mihai Iovea ^c

^a Technical University of Denmark, DTU Physics, 2800 Kgs. Lyngby, Denmark

^b Technical University of Denmark, DTU Compute, 2800 Kgs. Lyngby, Denmark

^c ACCENT PRO 2000 s.r.l. (AP2K), Nerva Traian 1, K6, Ap. 26, Bucharest 031041, S3, Romania

ARTICLE INFO

Keywords:

Spectral X-ray CT
Electron density
Effective atomic number
Joint reconstruction
Security screening

ABSTRACT

The development of energy resolving photon counting detectors (PCD) has paved the way to spectral X-ray Computed Tomography (CT), with which one can simultaneously extract the energy dependence of a material's linear attenuation coefficient (LAC). Spectral CT has proved to be an advanced technique to classify materials based on their physical properties such as electron density (ρ_e) and effective atomic number (Z_{eff}). However, the application of spectral CT may be hindered by the poor image reconstruction quality when used for material identification in security screening where rapid scanning is required. Image reconstruction from few projections or low radiation exposure time would enable rapid scanning. The reconstruction quality for each energy bin may also be degraded since the division of photon counts into multiple energy bins naturally leads to higher noise levels. In this work, we explore how to perform accurate spectral CT reconstructions from such data, and propose L_∞ -norm-based vectorial total variation (L_∞ -VTV) regularization that uses correlations between multiple energy bins. Using experimental data acquired with a custom laboratory instrument for spectral CT, the L_∞ -VTV is tested on "real life" phantoms consisting of materials in the range of $6 \leq Z_{\text{eff}} \leq 15$. For material classification from only 7 projections, the L_∞ -VTV gives the relative deviations of 3.5% for ρ_e and 2.4% for Z_{eff} , whereas the total nuclear variation (TNV) of another state-of-the-art joint reconstruction and the total variation (TV) yield those of 3.4% and 3.1%, and 3.8% and 4.2%, respectively. The L_∞ -VTV is now ready for use in security screening.

1. Introduction

Using sparse-view reconstructions from few projections in X-ray Computed Tomography (CT) systems can enable rapid scanning that is important for security applications. However, the poor reconstruction quality caused by the sparse data may hinder achieving the desired accuracy in material classification. Many studies have been done in addressing the sparse data problems either in CT systems or image processing. The total-variation (TV) introduced by Rudin, Osher, and Fatemi [1] has been effectively used for various image processing problems in noise suppression. TV regularization was shown to provide sharp discontinuities and preserve edges in image reconstruction, promoting sparse gradients of the images. Various TV based reconstruction algorithms have been implemented for sparse-view and limited angle CT [2,3]. Sidky et al. (2006) [4] implemented a TV-regularized

reconstruction in fan-beam CT for different insufficient data problems that consist of few-view projections and limited angles. They showed that the TV outperforms the existing reconstruction methods for such data.

The development of energy-resolved, photon counting detectors (PCD) led to the emergence of spectral CT [5–9], which can simultaneously retrieve the energy dependence of a material's linear attenuation coefficient (LAC). Thus, spectral CT is CT with information from different parts of the spectra separated into energy bins. The energy bins are defined from thresholds in the PCD. A photon is counted in a bin with a certain width if the collected charge from the photon is between the lower and upper threshold. Spectral CT with multiple energy bins may suffer from the fact that narrower energy bins integrate a lower number of photons and thus have significantly lower signal to noise ratios (SNR). To combat the heavy sparse-view artifacts and improve denoising

* Corresponding author at: Technical University of Denmark, DTU Physics, 2800 Kgs. Lyngby, Denmark.

E-mail addresses: doniyor.jumanazarov@fysik.dtu.dk (D. Jumanazarov), jakoo@dtu.dk (J. Koo), jake@fysik.dtu.dk (J. Kehres), hfp@fysik.dtu.dk (H.F. Poulsen), ullu@dtu.dk (U.L. Olsen), office@accent.ro (M. Iovea).

performance of spectral CT with low SNRs, we aim to implement and test the joint reconstruction algorithm in this work. The joint reconstruction algorithm jointly reconstructs the images by simultaneously employing the ensemble of the sinograms obtained for each energy bin, instead of reconstructing the images from each energy bin independently. For image processing problems, Blomgren and Chan (1998) [10] introduced a first definition of vectorial TV (VTV) regularizer that extends the conventional scalar TV into a multi-dimensional frame that considers dependency both in the spatial and spectral dimensions.

The main question when formulating a VTV as a convex regularizer is how to efficiently couple energy bins. Holt (2014) [11] investigated several VTV types with color image denoising experiments including Total Nuclear Variation (TNV). The TNV algorithm uses the nuclear norm in the gradients of images, which is the convex envelope of matrix rank [12]. Holt showed that minimizing the nuclear norm leads to promoting gradient vectors in different color channels to share common directions. The TNV leverages the structure coherence of a scanned object sharing the same structure information at various energies. Using spectral CT simulation data, Rigie et al. (2015) [13] applied TNV to reconstructing tissue density maps. They showed that TNV is better in suppressing noise and has less edge blurring compared to bin-by-bin TV reconstructions. Despite the fact that energy bins of spectral CT often have remarkably different noise levels, TNV showed robustness to undesired transfer of individual characteristics to other bins. With experimental data, Rigie et al. (2017) [14] implemented TNV, another VTV algorithm with the Frobenius norm and TV in dual-energy CT. They found that both VTV regularized couplings are better at suppressing noise compared to the conventional TV, while TNV was still the best regularizer among them. Zhong et al. [15] investigated a TNV reconstruction algorithm by combining energy-dispersive X-ray spectroscopy (EDS) with a more precise high-angle annular dark-field STEM (HAADF-STEM) tomography when the number of tilts is small or the photon counts are low. The TNV regularization was more precise in preserving features of reconstructed images compared to the simultaneous iterative reconstruction technique (SIRT) [16] and TV.

Miyata et al. [17] proposed using a L_∞ norm for defining VTV term. For an image denoising task, they showed that L_∞ -VTV can efficiently estimate the violation of inter-channel dependency and provide strong coupling among color channels. Duran et al. [18] analyzed several VTV regularizers by applying different collaborative norms to the discrete gradients of multi-channel images consisting of a 3D matrix, whose dimensions correspond to color channels, the spatial gradients in x and y-axis, and the image pixels. For color image denoising, they demonstrated that the L_∞ -VTV and TNV can give the better results to suppress color artifacts compared to the other VTV norms, and the efficiency of particular norm appeared to be dependent on the experimental data considered.

In previous work [19], we presented a method for system-independent material classification through attenuation decomposition (SIMCAD) from spectral CT. The SIMCAD estimates the system-independent material properties such as electron density (ρ_e) and effective atomic number (Z_{eff}) from the energy-dependent LACs, independent of the system or the scanner specification like the X-ray spectrum. This method employs the attenuation decomposition introduced by Alvarez et al. [20] for the method formulation and adopts it for multi-energies.

Data with low SNRs in each energy bin and data acquired with few projections result in poorly reconstructed images. Employing advanced reconstruction algorithms, an accurate reconstruction can be performed from such data. In this work, we therefore implement a L_∞ norm-based VTV joint reconstruction algorithm in spectral CT based on experimental data acquired with a custom laboratory instrument. L_∞ -VTV uses the infinity (maximum) norm to jointly penalize the maximum image gradient magnitudes over multiple energy bins. This joint reconstruction algorithm has a positive weighting parameter that controls the balance between a good fit to energy-resolved sinogram data and a smooth

reconstruction. This parameter determines the strength of the regularization term. We compare the reconstruction and classification performances of L_∞ -VTV with those of TNV and TV, based on figures of merit (FOM) such as the correlation coefficient and the SIMCAD method. The correlation coefficient evaluates the reconstructed image quality against ground-truth images. The FOMs are estimated for different numbers of projections and different photons statistics as a function of the weighting parameter.

The robustness of each algorithm to high noise added to certain energy bins is also tested. With an attention to security screening, the classification performance of each algorithm is tested on a broad range of materials, with 20 different materials for the calibration step and 15 additional materials for (ρ_e, Z_{eff}) calculation. We expect that the improvement in the reconstruction quality leads to more accurate extraction of LACs, and thereby to better material classification.

The proposed joint reconstruction algorithm is demonstrated in a fan-beam geometry, but the algorithm can be easily implemented in a three-dimensional (3D) cone or parallel beam geometry for 3D CT imaging. This can be done by imposing the regularization slice by slice or by considering spatial regularization in 3D. This can be a powerful quantitative tool for exploring complex connections between the features and microstructure of materials in material science [21,22]. Thus, the improvement in estimating (ρ_e, Z_{eff}) distribution based on the image reconstruction can be useful for studying the complex microstructure of materials. Moreover, the reconstruction algorithm introduced in this study can also be applied to data from a variety of spectral imaging techniques such as visible light, electron or neutron tomography.

2. Experimental setup. Data processing

2.1. Physical properties of materials

The LAC is proportional to a material's electron density [23], represented by the number of electrons per unit volume (electron – mole/cm³). For a compound or mixture that has the composition with the total number of different elements N , the electron density can be calculated as

$$\rho_e = \frac{\sum_{i=1}^N \alpha_i Z_i}{\sum_{i=1}^N \alpha_i A_i} \rho, \quad (1)$$

where ρ is mass density (g/cm³), A_i and Z_i are atomic mass and atomic number for each element i , respectively, and α_i represents the number of atoms that have atomic number Z_i . For compounds, the atomic number is referred to as effective atomic number, Z_{eff} and a now classical parameterization is defined as [24,25].

$$Z_{\text{eff}} = \sqrt[l]{\sum_{i=1}^N r_i Z_i}, \quad (2)$$

where r_i is “relative electron fraction” contribution of an element i , which is determined as

$$r_i = \frac{\alpha_i Z_i}{\sum_{j=1}^N \alpha_j Z_j}.$$

In previous work [19], the exponent l was investigated to tune this value on the best match for material classification depending on the materials, source spectrum and system features. The $l = 8.0$ was found to be the optimal value for classification performance, therefore we choose this value for the calculation of reference Z_{eff} values in this work.

2.2. Experimental setup and materials

The experiments were performed in the 3D Imaging Center at DTU, Denmark. Fig. 1 illustrates the experimental setup. Table 1 lists the parameters of the experimental setup designed for spectral CT

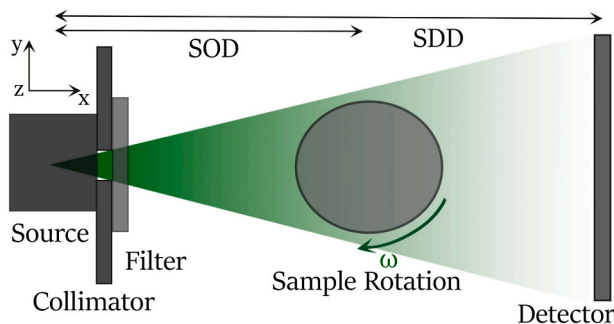


Fig. 1. Illustration of the experimental setup.

Table 1
Parameters of the experimental setup.

Source parameters	150 kV, 0.5 mA
Focal spot	75 μm
Number of pixels	1 \times 640 1D array
Pixel size	0.8 \times 0.8 mm^2
Detector resolution	6.5% (8 keV at 122 keV)
Number of energy bins	128 (1.1 keV width each)
Number of projections	7, 12, 36
Total integration time per projection	2 ms, 10 ms, 50 ms, 100 ms, 8 s
Source to detector distance (SDD)	701 mm
Source to sample distance (SOD)	500 mm

measurements. The X-ray beam was generated by a micro focused X-ray source of the type L12161–07 made by Hamamatsu. The operating parameters such as the acceleration tube voltage and anode filament current were 150 kV and 0.5 mA, respectively. A 2-mm-thick aluminum filter was placed in front of the source to remove photons with energies below the detector's energy range. The incident beam was collimated to a fan beam by using a JJ X-Ray IB-C80-AIR slit with 5-mm-thick tungsten carbide blades to fully illuminate all the detector pixels. This helps keep the beam size to a minimum, and thereby reduce the background radiation composed of scattered and fluorescent photons. The sample placed on the rotation stage was scanned between discrete rotations with different increments over a range of 360 degrees depending on the number of projections. The source to detector distance (SDD) is 701 mm, whereas the source to sample distance (SOD) is 500 mm.

The detector used to conduct the experiments is MultiX ME-100 v2 produced by Detection Technology S.A.S. in Moirans, France. We employ a system of five detector modules, each module is composed of a 1 \times 128 line array of pixels, each with size of 0.8 \times 0.8 mm^2 . Each pixel has the ability to acquire data in total 128 energy bins, each with width of 1.1 keV, evenly spaced between 20 and 160 keV. The energy resolution of the detector with high X-ray fluxes is 6.5% (8 keV at 122 keV) [27]. The detector is made up of a 3-mm-thick CdTe sensor. Incoming

photons pass through a collective cathode of a continuous metal film. The sensor has pixelated anodes on the other side with notably smaller size, which are placed on readout electronics. A single MultiX detector has 128 pixelated anodes (pixels) with a pitch of 800 μm and consists of an array of 4 sensor crystals, each with 32 pixels. The detector can operate with integration time from 2 ms to 100 ms (in 10 μs increments). The lower integration time indicates the lower photon counts in each energy bin.

Fig. 2 shows examples of samples scanned and processed through each reconstruction algorithm, which contain multiple materials scanned in groups. Table 2 and Table 3 list the reference and test materials, which are used for the calibration step and (ρ_e, Z_{eff}) calculation in material classification described in Section 4, respectively. The reference ρ_e and Z_{eff} values in the tables were calculated by Eq. (1) and Eq. (2), with the exponent $l = 8.0$. Sample dimensions are shown as diameter for circular samples or as width \times length for rectangular samples. The plastic materials found in both tables are polyvinylidene fluoride (PVDF), polyoxymethylene-H (POM–H), polyethylene terephthalate (PET), polytetrafluoroethylene (PTFE), polyoxymethylene-C (POM–C), polymethyl methacrylate (PMMA) and polycarbonate (PC). Most materials listed are explosive or precursor materials, and prohibited in checked-in or carry-on luggage. The materials correspond to the range of $6 \leq Z_{\text{eff}} \leq 15$, which covers most of the materials encountered in security screening [28]. The materials used do not possess K-edges within the detector's energy range. If materials present K-edge absorption in the LAC, the bins with energies lower than the K-edge would be truncated making it consistent with the formulation of the classification method presented in Section 4.

2.3. Data correction, energy bins rebinning and sinogram

The physical effects in the detector sensor, such as charge sharing and weighting potential cross-talk, fluorescence radiation, Compton scattering radiation, pulse pile up and incomplete charge collection, distort the measured spectra, and thereby lead to strong deviations of spectral LACs from the expected attenuation values. Therefore, the detector's distorted spectral response is corrected with the correction algorithm proposed by Dreier et al. [30]. The distorted LACs cannot be completely restored at low- and high-energies because of complete radiation attenuation by a sample, leading to photon starvation. Therefore, we truncate bins in which the LAC is not restored, and set the low- and high-energy thresholds, corresponding to 33.2 keV and 132.4 keV, respectively [19].

The correction of the raw data is followed by energy bins rebinning. The detector has 90 energy bins between the low- and high-energy thresholds. The data is rebinned into a smaller number of bins to increase photons statistics of each bin, by merging photon counts between the low- and high-energy thresholds. In previous work [19], the classification performance was tested for optimized bi-, 6, 15, 30, 45 and 90 energy bins. The results showed that 30, 45 and 90 energy bins did not

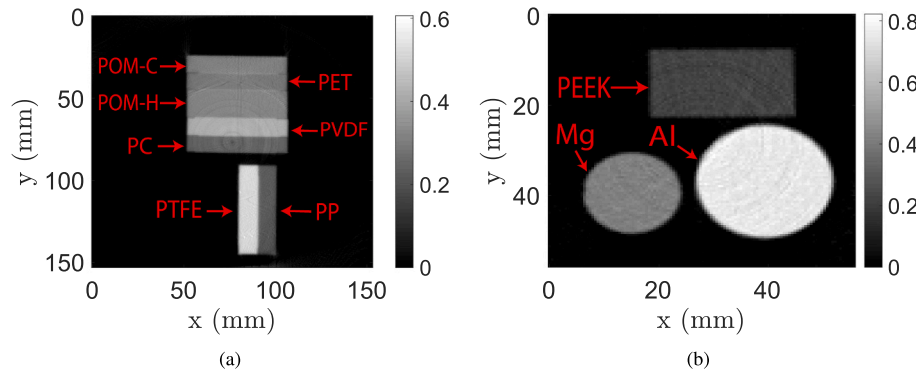


Fig. 2. Examples of samples used to conduct the experiments, reconstructed with SIRT from 360 projections for illustration. The gray scale bars represent the LACs (cm^{-1}). (a) Sample containing the plastics indicated by red arrows, presented for 42 keV. The polypropylene (PP) material is excluded in the classifications since it is mixed with chemical colorants, leading to a higher Z_{eff} value than the pure PP [26]. (b) Sample containing aluminum, magnesium and polyetheretherketone (PEEK), presented for 61.9 keV. (For interpretation of the references to color in this figure legend, the reader is referred to the web version of this article.)

Table 2

The reference materials composing the different samples scanned and used for the calibration step in material classification, described in the Subsection 4.1. The mass density, ρ for the plastic materials was measured with uncertainties of $\pm 0.15\%$. The mass densities for the rest of materials represent the theoretical values found in PubChem data [29].

Material	Chemical formula	Width×length/diameter (mm)	ρ (g/cm ³)	ρ_e (e ⁻ mol/cm ³)	Z_{eff}
Graphite	C	12.7	1.8	0.899	6
PC	(CO ₃ C ₁₃ H ₈) _n	8.2 × 53.5	1.18	0.610	6.82
PMMA	(C ₅ O ₂ H ₈) _n	40 × 42	1.18	0.636	7.02
POM-C	(CH ₂ O) _n	9 × 53.5	1.41	0.753	7.40
PTFE	(C ₂ F ₄) _n	9 × 53.3	2.16	1.035	8.70
<i>N,N</i> -Dimethylhydrazine	C ₂ H ₈ N ₂	67	0.791	0.447	6.44
Ethylenediamine	C ₂ H ₈ N ₂	67	0.90	0.509	6.44
Acetone 2	C ₃ H ₆ O	54	0.785	0.432	6.90
Nitrobenzene	C ₆ H ₅ NO ₂	49	1.20	0.624	7.00
Ethanol 96%	C ₂ H ₅ O (96%)	67 × 67	0.798	0.450	7.06
Methanol	CH ₃ OH	20	0.792	0.446	7.29
Hydrazine solution	H ₄ N ₂ (35%)	54	1.0	0.561	7.43
Nitromethane	CH ₃ NO ₂	20	1.14	0.597	7.50
Water	H ₂ O	20	0.997	0.554	7.78
Water 3	H ₂ O	12.7	0.997	0.554	7.78
Hyd. Peroxide 2	H ₂ O ₂ (50%)	73 × 74	1.22	0.661	7.83
Magnesium 2	Mg	18	1.74	0.859	12
Aluminum 2	Al	25	2.70	1.3	13
Aluminum 3	Al	20 × 20	2.70	1.3	13
Silicon	Si	25	2.33	1.161	14

Table 3

The test materials composing the different samples scanned and used for (ρ_e , Z_{eff}) calculation in material classification, described in the Subsection 4.2. The mass density, ρ for the plastic materials was measured with uncertainties of $\pm 0.15\%$. The mass densities for the rest of materials represent the theoretical values found in PubChem data [29].

Material	Chemical formula	Width×length/diameter (mm)	ρ (g/cm ³)	ρ_e (e ⁻ mol/cm ³)	Z_{eff}
PET	(C ₁₀ H ₈ O ₄) _n	9 × 53.5	1.39	0.721	7.09
POM-H	(CH ₂ O) _n	15.5 × 53.3	1.43	0.763	7.40
PVDF	(C ₂ H ₂ F ₂) _n	9 × 53.5	1.79	0.896	8.40
PTFE 2	(C ₂ F ₄) _n	12.7	2.2	1.056	8.70
2-butanone	C ₄ H ₈ O	83	0.805	0.447	6.76
Acetone	C ₃ H ₆ O	20	0.785	0.432	6.90
Methanol 2	CH ₃ OH	81	0.792	0.446	7.29
Ethanol	C ₂ H ₆ O	67 × 67	0.947	0.532	7.63
40%	(40%)				
Water 2	H ₂ O	51 × 51	0.997	0.554	7.78
Nitric acid	HNO ₃	83	1.39	0.714	7.80
(65%)					
Hyd.	H ₂ O ₂ (50%)	20	1.22	0.661	7.83
Peroxide					
Magnesium	Mg	12.7	1.74	0.859	12
Aluminum	Al	25	2.70	1.3	13
Silicon powder	Si	48	0.65	0.324	14
Silicon 2	Si	12.7	2.33	1.161	14

improve classification performance compared to the 15 energy bins approach. The reasons for this may be that firstly the width of each energy bin becomes narrower than the detector's energy resolution when employing a larger number of bins; Secondly the detector noise in each bin increases as the width of each bin decreases. Therefore, in this work we use 15 energy bins, which are distributed uniformly between the low- and high-energy thresholds, i.e. each with equal width.

We generate the ensemble of sinograms (or line integrals) obtained for each energy bin after the energy bins rebinning step, based on Lambert–Beer's law as follows:

$$I_k(\vec{x}) = -\log \frac{I_k(\vec{x})}{I_{0,k}(\vec{x})}, \quad k = 1, 2, 3, \dots, 15; \quad (3)$$

where $I_{0,k}$ denotes the flat-field photon counts for energy bin k , i.e. the projection captured by the detector without the sample, and I_k is the photon counts for energy bin k , measured with the sample being

inserted. \vec{x} represents the 1D detector pixel array.

3. Reconstruction algorithms

3.1. Problem formulation

Suppose spectral CT measurements consist of N sinograms $\mathbf{p}_1, \dots, \mathbf{p}_N \in \mathbb{R}^M$ where N and M represent the number of energy bins and the number of detector pixels times the number of projection angles, respectively. From the energy-resolved sinograms, we aim to reconstruct the corresponding N images $\mathbf{u}_1, \dots, \mathbf{u}_N \in \mathbb{R}^J$ representing the LACs for each energy bin E_i ($i = 1, 2, \dots, N$), where J is the number of pixels per each image. For notational simplicity, we define the stack of sinograms as a vector $\mathbf{p} \in \mathbb{R}^{NM}$ and the stack of N images as $\mathbf{u} \in \mathbb{R}^{NJ}$, and we denote the LAC for energy bin E_i on the j^{th} pixel ($j = 1, 2, \dots, J$) by $u_{i,j}$.

The forward-projection to map an image to the sinogram domain can be modeled by a linear operator A such that $A\mathbf{u}_i$ estimates a sinogram for each energy bin E_i . By stacking the same operator for all energy bins, we define the linear operator A on the stack of images \mathbf{u} such that $A\mathbf{u} = \mathbf{p}$. Then, a typical reconstruction approach is to minimize the data fidelity term defined as the squared reprojection error that is l_2 norm of the difference between the computed ($A\mathbf{u}$) and measured sinogram data (\mathbf{p}). Thus, the data fidelity term can be expressed as

$$\mathcal{G}(A\mathbf{u}) = \|A\mathbf{u} - \mathbf{p}\|_2^2. \quad (4)$$

This data fidelity term may not be sufficient for performing accurate reconstructions, as data can be highly noisy or obtained from a small number of projections. To reconstruct high-quality images, we need a robust regularization scheme, by imposing prior knowledge on the solutions.

One can independently apply (isotropic) total variation regularization on each energy bin E_i , which can be written as

$$\mathcal{R}_{\text{TV}}(\mathbf{u}_i) = \sum_{j=1}^J \sqrt{\partial_x u_{i,j}^2 + \partial_y u_{i,j}^2}, \quad (5)$$

where $\partial_x u_{i,j}$ and $\partial_y u_{i,j}$ are the gradients of the image \mathbf{u}_i for the pixel j with respect to x and y axis, respectively. This TV regularization term does not exploit any correlation between the images from different energy bins.

A more robust regularization can be achieved by correlating the gradients of the images from different energy bins. One way to exploit

the inter-bin correlations of the image gradients is Total Nuclear Variation (TNV) regularization [13,18], which is common to all energy bins and defined as the sum of nuclear norm of the Jacobian matrix over all image pixels:

$$\mathcal{R}_{\text{TNV}}(\mathbf{u}) = \sum_{j=1}^J \left\| \begin{pmatrix} \partial_x u_{1,j} & \partial_y u_{1,j} \\ \partial_x u_{2,j} & \partial_y u_{2,j} \\ \vdots & \vdots \\ \partial_x u_{N,j} & \partial_y u_{N,j} \end{pmatrix} \right\|_*, \quad (6)$$

where the nuclear norm $\|\cdot\|_*$ of the Jacobian matrix including image gradients in pixel, spatial and energy dimension is the sum of its singular values. TNV can be degenerate when there are some outliers in the gradients of the images.

To overcome the disadvantage of TNV, we suggest to use another VTV regularization based on L_∞ (infinity) norm, which is the sum of the maximum of gradients among N energy bins over all image pixels, defined as

$$\begin{aligned} \mathcal{R}_{L_\infty-\text{VTV}}(\mathbf{u}) &= \|\mathbf{Du}\|_{\infty,1,1} \\ &:= \sum_{j=1}^J \left(\max_{1 \leq i \leq N} |\partial_x u_{i,j}| + \max_{1 \leq i \leq N} |\partial_y u_{i,j}| \right), \end{aligned} \quad (7)$$

where \mathbf{D} is a linear operator for the discrete gradient operations such that \mathbf{Du} is a 3D matrix. That is, $(\mathbf{Du})_{i,j,l}$ represents the gradient of the image \mathbf{u}_i for the pixel j with respect to x axis when $l = 1$ or y axis when $l = 2$. We use the notation $\|\cdot\|_{\infty,1,1}$, as it involves applying the L_∞ norm along the energy bins dimension, and l_1 norm along the other dimensions with respect to the spatial (pixel) locations and the spatial gradient directions [18]. This L_∞ -VTV norm correlates the gradients strongly over multiple energy bins, while disallowing some outliers in the sense of the gradient magnitudes. This property will be illustrated in the Subsection 5.4.

By combining the data fidelity term (Eq. (4)) and the regularization term L_∞ -VTV (Eq. (7)), we formulate the optimization problem that we want to solve:

$$\min_{\mathbf{u} \geq 0} \frac{\lambda}{2} \mathcal{G}(\mathbf{Au}) + \mathcal{R}_{L_\infty-\text{VTV}}(\mathbf{u}), \quad (8)$$

where λ is the weighting parameter between the two terms. Here, we impose the non-negativity constraint on \mathbf{u} , as the LACs are desired to be non-negative.

3.2. Optimization

We describe the optimization of our objective function defined in Eq. (8). Although the objective function is convex, the challenge lies in having the composite operators \mathbf{A} in the data fidelity term and \mathbf{D} in the regularization term. To deal with such difficulty, we employ an efficient primal dual algorithm, called Hybrid Gradient Primal Dual method (HGPD) [31]. The basic idea of primal dual algorithms is to reformulate a minimization problem as a minimization-maximization (min-max) problem and aim to find the saddle point. To derive the min-max problem, primal dual algorithms rely on the Fenchel conjugate function [31] F^* of a convex function F , defined by

$$F^*(\mathbf{y}) = \sup_{\mathbf{x}} \langle \mathbf{x}, \mathbf{y} \rangle - F(\mathbf{x}). \quad (9)$$

To use the primal dual algorithm, we introduce two dual variables \mathbf{q} and \mathbf{r} corresponding to the operators \mathbf{A} and \mathbf{D} , respectively. To rewrite the original minimization problem defined in Eq. (8) as a saddle point problem, we use the Fenchel conjugate function to obtain

$$\mathcal{G}(\mathbf{Au}) = \max_{\mathbf{q}} \langle \mathbf{Au}, \mathbf{q} \rangle - \mathcal{G}^*(\mathbf{q}), \quad (10)$$

$$\mathcal{R}_{\text{VTV}}^{\text{L}_\infty}(\mathbf{Du}) = \max_{\mathbf{r}} \langle \mathbf{Du}, \mathbf{r} \rangle - \mathcal{R}^*(\mathbf{r}), \quad (11)$$

where \mathcal{G}^* and \mathcal{R}^* are the conjugate functions of

$$\mathcal{G}(\mathbf{x}) = \frac{1}{2} \|\mathbf{x} - \mathbf{p}\|_2^2, \quad (12)$$

$$\mathcal{R}(\mathbf{X}) = \|\mathbf{X}\|_{\infty,1,1}. \quad (13)$$

Based on Eq. (10) and Eq. (11), we now turn the minimization problem of Eq. (8) into the following saddle point problem

$$\min_{\mathbf{u}} \max_{\mathbf{q}, \mathbf{r}} \langle \mathbf{Au}, \mathbf{q} \rangle + \langle \mathbf{Du}, \mathbf{r} \rangle - \mathcal{G}^*(\mathbf{q}) - \mathcal{R}^*(\mathbf{r}) + \delta_+(\mathbf{u}), \quad (14)$$

where δ_+ is the indicator function for the non-negative constraint, defined by

$$\delta_+(\mathbf{x}) = \begin{cases} x & \text{if } x \geq 0, \\ \infty & \text{if } x < 0. \end{cases} \quad (15)$$

HGPD provides an efficient way to solve the saddle point problem, by alternatively updating the primal and dual variables as follows:

$$\mathbf{u}^{k+1} = \text{prox}_{\delta_+}(\mathbf{u}^k - \tau(\mathbf{A}^T \mathbf{q}^k + \mathbf{D}^T \mathbf{r}^k)), \quad (16)$$

$$\bar{\mathbf{u}} = 2\mathbf{u}^{k+1} - \mathbf{u}^k, \quad (17)$$

$$\mathbf{q}^{k+1} = \text{prox}_{\sigma_1 \mathcal{G}^*}(\mathbf{q}^k + \sigma_1 \mathbf{A} \bar{\mathbf{u}}), \quad (18)$$

$$\mathbf{r}^{k+1} = \text{prox}_{\sigma_2 \mathcal{R}^*}(\mathbf{r}^k + \sigma_2 \mathbf{D} \bar{\mathbf{u}}), \quad (19)$$

where k is the iteration number, τ is the step size for the primal variable, σ_1, σ_2 are the step sizes for the dual variables and prox is the proximal operator [32] defined by

$$\text{prox}_{\sigma f}(\mathbf{x}) = \underset{\mathbf{y}}{\operatorname{argmin}} \frac{1}{2\sigma} \|\mathbf{x} - \mathbf{y}\|_2^2 + f(\mathbf{x}). \quad (20)$$

In Algorithm 1, we provide the whole procedure of optimization, where $\|\mathbf{A}\|_2$ denotes the operator norm of \mathbf{A} , which is the largest eigenvalue of \mathbf{A} . To guarantee the convergence, following [31] we carefully choose the step sizes based on the operator norms, which can be computed by the power method [33]. The concrete solutions to Eq. (16) and Eq. (18) are provided in Eq. (24) and Eq. (26), respectively. To evaluate hgp4, we use the fact that the proximal operator to L_∞ norm is the projection operator to L_1 unit ball, denoted by $\Pi_{\|\cdot\| \leq 1}$ [32]. Then, we can write the solution to Eq. (19) as follows:

$$(\text{prox}_{\sigma_2 \mathcal{R}^*}(\mathbf{V}))_{i,j,l} = \text{sgn}(\mathbf{V}_{i,j,l}) \Pi_{\|\cdot\| \leq 1}(\sigma_2 \|\mathbf{V}_{i,j,l}\|), \quad (21)$$

where sgn is the sign function, i and j denote the indices for the energy bin and image pixel, respectively, and $l \in \{1, 2\}$ denotes the index for the gradient with respect to x or y axis. The notation $\mathbf{V}_{:,j,l}$ represents a vector consisting of the elements with respect to the energy bins, given j and l . We refer to [18] for a detailed derivation.

To check the convergence, we introduce two residuals \mathcal{P} and \mathcal{D} for the primal variables and the dual variables, respectively, as follows:

$$\begin{aligned} \mathcal{P}^{k+1} &= \|\mathbf{u}^k - \mathbf{u}^{k+1}\| / \tau - \mathbf{A}^T (\mathbf{q}^k - \mathbf{q}^{k+1}) \\ &\quad - \mathbf{D}^T (\mathbf{r}^k - \mathbf{r}^{k+1}) \|_1, \end{aligned} \quad (22)$$

$$\begin{aligned} \mathcal{D}^{k+1} &= \|\mathbf{q}^k - \mathbf{q}^{k+1}\| / \sigma_1 - \mathbf{A} (\mathbf{u}^k - \mathbf{u}^{k+1}) \|_1 \\ &\quad + \|\mathbf{r}^k - \mathbf{r}^{k+1}\| / \sigma_2 - \mathbf{D} (\mathbf{u}^k - \mathbf{u}^{k+1}) \|_1. \end{aligned} \quad (23)$$

These primal and dual residuals measure the changes of the solutions per iteration for primal and dual variables, respectively. Such residuals are expected to decrease with the iterations. The behaviors of these residuals and the stopping criteria will be discussed in the Subsection 5.1.

Algorithm 1. Primal dual updates for solving Eq. (14).

Set the step sizes:

$$\tau = \frac{1}{\|\mathbf{A}\|_2 + \|\mathbf{D}\|_2}, \quad \sigma_1 = \frac{1}{\|\mathbf{A}\|_2}, \quad \sigma_2 = \frac{1}{\|\mathbf{D}\|_2}.$$

Initialize $\mathbf{u}^0, \mathbf{q}^0, \mathbf{r}^0$ as zero vectors.

for $k = 0, 1, 2, \dots$

$$\mathbf{u}^{k+1} = \max(\mathbf{u}^k - \tau(\mathbf{A}^T \mathbf{q}^k + \mathbf{D}^T \mathbf{r}^k), 0), \quad (24)$$

$$\bar{\mathbf{u}} = 2\mathbf{u}^{k+1} - \mathbf{u}^k, \quad (25)$$

$$\mathbf{q}^{k+1} = \frac{\mathbf{q}^k + \sigma_1(\mathbf{A}\bar{\mathbf{u}} - \mathbf{p})}{1 + \sigma_1}, \quad (26)$$

$$\mathbf{r}^{k+1} = \text{prox}_{\sigma_2 R^*}(\mathbf{r}^k + \sigma_2 \mathbf{D}\bar{\mathbf{u}}). \quad (27)$$

3.3. Correlation coefficient

We estimate the reconstruction quality based on the correlation coefficient r , which measures how the reconstructed image \mathbf{u} is linearly connected to the ground-truth (true) image \mathbf{v} , and it is expressed for the energy bin i as

$$r_i = \frac{\sum_j (u_j - \bar{u})(v_j - \bar{v})}{\sqrt{\sum_j (u_j - \bar{u})^2 \sum_j (v_j - \bar{v})^2}}, \quad (28)$$

where \bar{u} and \bar{v} are the mean LACs calculated from the LACs for each pixel, and u_j and v_j are the j^{th} pixel values of \mathbf{u} and \mathbf{v} , respectively. In this work, to compute correlation coefficients the ground-truth images of a sample at multiple energy bins are synthetically created by assigning the corresponding mean LAC to each energy bin for each material in the sample. The mean LAC for each energy bin is extracted from the attenuation value histogram based on the normal distribution after sample reconstruction with SIRT from 360 projections [19].

4. Classification method

The SIMCAD method that estimates material features ρ_e and Z_{eff} from spectral CT is described in detail by Jumanazarov et al. [19], and is briefly repeated in this section for the convenience of the reader.

4.1. Calibration step

The LAC for the material m , and for the energy bin E_k can be defined as [20].

$$\mu_m(E_k) = \rho_{e,m} \left(Z_{\text{eff},m}^{n-1} p(E_k) + c(E_k) \right), \quad (29)$$

where $m = 1, 2, \dots, M$, $k = 1, 2, \dots, K$ with M and K which represent the total number of materials and energy bins, respectively. Note that we use 15 energy bins as discussed in the Subsection 2.3. $p(E_k)$ and $c(E_k)$ are photoelectric absorption and Compton scattering basis functions for energy bin E_k , respectively.

To optimize the basis functions and the exponent n , we define the non-linear objective function as:

$$\min_{0 \leq p_1, c_1, \dots, p_K, c_K, n} \sum_{m=1}^M \sum_{k=1}^K \left(\mu_m(E_k) - \rho_{e,m} \left(Z_{\text{eff},m}^{n-1} p_k + c_k \right) \right)^2, \quad (30)$$

where $p_k = p(E_k)$ and $c_k = c(E_k)$. The objective function is optimized by using a nonlinear least square solver based on the trust region method [34]. We impose initial positivity constraints as $p_k^0 = 0.5$, $c_k^0 = 0.5$ and $n^0 = 3.6$ for all k . The classification results were found to be independent from the initial constraints. The classification method can be formulated

for any number of energy bins. The energy-dependent basis functions and the exponent n are calibrated by using the reference ρ_e and Z_{eff} values of the reference materials listed in Table 2, and are the same for all the materials being estimated.

4.2. Calculation of material features

The basis functions and the exponent n which are defined in the calibration step are employed to compute ρ_e and Z_{eff} values of the test materials listed in Table 3. We reformulate the LACs defined in Eq. (29) as a linear system of equations as follows

$$\begin{pmatrix} \bar{p} & \bar{c} \\ & \ddots \\ & \bar{p} & \bar{c} \end{pmatrix} \begin{pmatrix} z_1 \\ \rho_{e,1} \\ \vdots \\ z_M \\ \rho_{e,M} \end{pmatrix} = \begin{pmatrix} \bar{\mu}_1 \\ \vdots \\ \bar{\mu}_M \end{pmatrix} \quad (31)$$

where z_m is a temporary variable inserted instead of $\rho_{e,m} Z_{\text{eff}}^{n-1}$ and $\bar{p} = (p_1, \dots, p_K)^T$, $\bar{c} = (c_1, \dots, c_K)^T$ and $\bar{\mu}_m = (\mu_m(E_1), \dots, \mu_m(E_K))^T$. $\mu_m(E_k)$ represents the extracted LACs of the test material m for the energy bin E_k . The linear matrix has the size of $(M \times K)$ -by- $(2 \times M)$ and the number of unknowns is $2 \times M$. Using the positivity constraint on the solution we retrieve the vector $(z_1, \rho_{e,1}, \dots, z_M, \rho_{e,M})$ minimizing the norm in the linear least square problem. From this, Z_{eff} values are calculated for all the test materials m as

$$Z_{\text{eff},m} = \left(\frac{z_m}{\rho_{e,m}} \right)^{\frac{1}{n-1}}. \quad (32)$$

The material classification accuracy is defined as the percent relative deviation from the reference values for ρ_e and Z_{eff} as

$$\Delta Z_{\text{eff}}^{\text{rel}} = 100\% \cdot \frac{Z_{\text{eff}}^{\text{est}} - Z_{\text{eff}}^{\text{ref}}}{Z_{\text{eff}}^{\text{ref}}}, \quad (33)$$

$$\Delta \rho_e^{\text{rel}} = 100\% \cdot \frac{\rho_e^{\text{est}} - \rho_e^{\text{ref}}}{\rho_e^{\text{ref}}}, \quad (34)$$

where superscripts est and ref denote the estimated and reference values, respectively.

5. Results and discussions

In this section we present and discuss the results obtained with the different reconstruction algorithms based on spectral CT measurements. Note that the correlation coefficients calculated as a function of the iteration number and weighting parameter represent the mean values calculated from the coefficients for the 15 energy bins used.

5.1. Stopping criterion to terminate the iterations

The results presented in this subsection were obtained using the experimental sample illustrated in Fig. 2a. The sample was scanned with the total exposure time of 8 s, which gives an effective frame rate of 80 frames for each projection, as the integration time for each frame is set to 100 ms. The reconstructions were performed from 36 projections. The weighting parameters λ used to reproduce the results correspond to the maximal correlation coefficients as the optimal reconstruction for each algorithm, which are shown in Fig. 5. Fig. 3 shows the sum of primal and dual residuals for each reconstruction algorithm. As expected, the sum decreases as the number of iterations increases for each algorithm, which ensures the convergence of the algorithms. The L_∞ -VTM reconstruction converges noticeably faster than the TNV and the TV with the slowest convergence rate.

We also examine the convergence of each algorithm based on the correlation coefficient. Fig. 4 presents the correlation coefficients as a

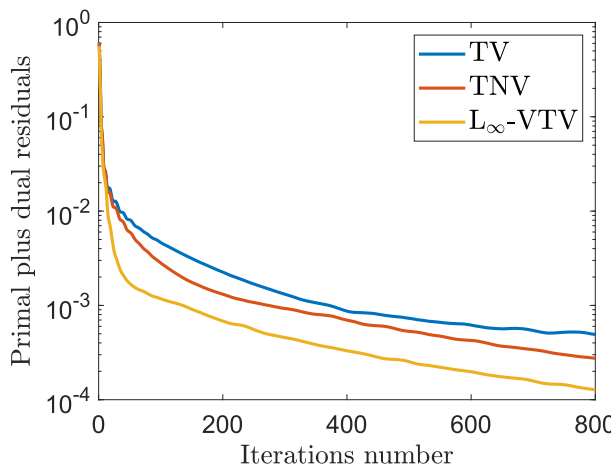


Fig. 3. The sum of the primal and dual residuals as a function of the iteration number for different reconstruction algorithms.

function of the iteration number for 7 and 36 projections. For L_∞ -VTV, TNV and TV, we stop the iterations at the point where both the correlation coefficient and its gradient remain stable. The iterations for SIRT can be terminated when the correlation coefficient reaches the maximal value. Thus, the correlation coefficient can be a tool indicating the convergence of the reconstruction to the ground-truth image. **Table 4** shows the number of iterations fixed for each algorithm and for each number of projections based on the correlation coefficients.

5.2. Reconstruction from a decreasing number of projections

The results presented in this subsection were obtained using the sample illustrated in Fig. 2a, which was scanned with the total exposure time of 8 s per projection, and with different numbers of projections. **Fig. 5** presents the correlation coefficients as a function of weighting parameters for different numbers of projections. A too small λ value results in an over-regularized image with blurred edges, while a too large value leads to insufficient regularization effects, as notable in Eq. (8). For the 36-projection case, in which the data quality is relatively better, the maximal correlation coefficients appear to be closer for each algorithm than the coefficients for the 12- and 7-projection cases. For the 12- and 7-projection cases, the maximal correlation coefficients for the L_∞ -VTV are significantly higher than those for the other algorithms. The joint TNV regularization also gives higher correlation coefficients than the bin-by-bin TV and SIRT reconstructions.

Fig. 6 compares the TV, TNV and L_∞ -VTV reconstructions for 36, 12 and 7 projections, each corresponding to the maximal correlation coefficient as the optimal reconstruction. For the limited 12- and 7-projection cases, the TNV and L_∞ -VTV joint reconstructions appear to have clearly less structural artifacts than the TV reconstruction that suffers

from over-smoothing and more distortion in shape. Comparing the L_∞ -VTV with the TNV for the limited-projection cases, we notice that the former one presents more accurate reconstructions with better structures and preserved edges than the latter one.

5.3. Reconstruction for decreasing radiation dose levels

We explore the effect of decreasing the integration time and thereby reducing radiation dose levels for spectral CT scans on reconstruction quality for each algorithm. This can be particularly important for medical imaging that requires keeping radiation doses to patients as low as possible. The results presented in this subsection were reproduced employing the sample illustrated in Fig. 2b. The sample was scanned with different detector integration times to test the robustness of each algorithm to data with low signal-to-noise ratios in each energy bin. Note that the total exposure time was set equal to the integration time for each projection. The reconstructions were performed from 36 projections. **Fig. 7** shows the correlation coefficients as a function of

Table 4

The number of iterations fixed for each algorithm and for each of the selected number of projections.

Projection number	SIRT	TV	TNV	L_∞ -VTV
7	80	550	750	550
12	80	550	600	500
36	100	400	500	400
360	150	400	400	400

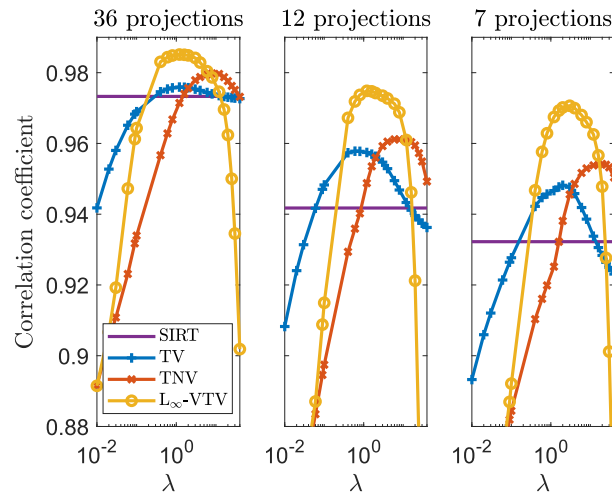


Fig. 5. Correlation coefficients as a function of weighting parameter λ for different numbers of projections. Note the logarithmic scale in the x-axis.

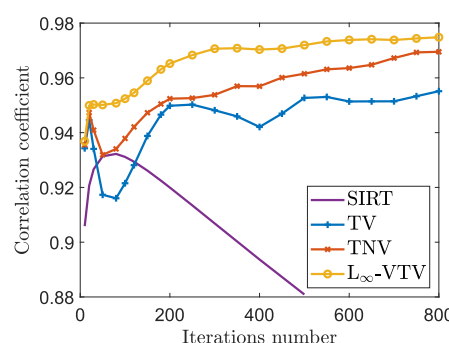
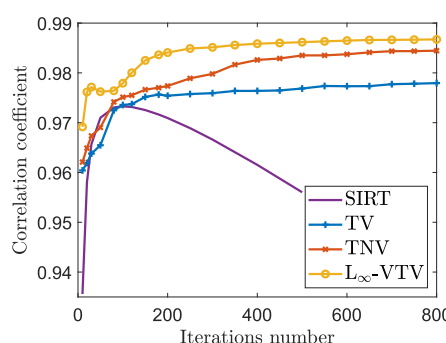


Fig. 4. Correlation coefficients as a function of the iteration number for different reconstruction algorithms, computed for 36 (left) and 7 projections (right).

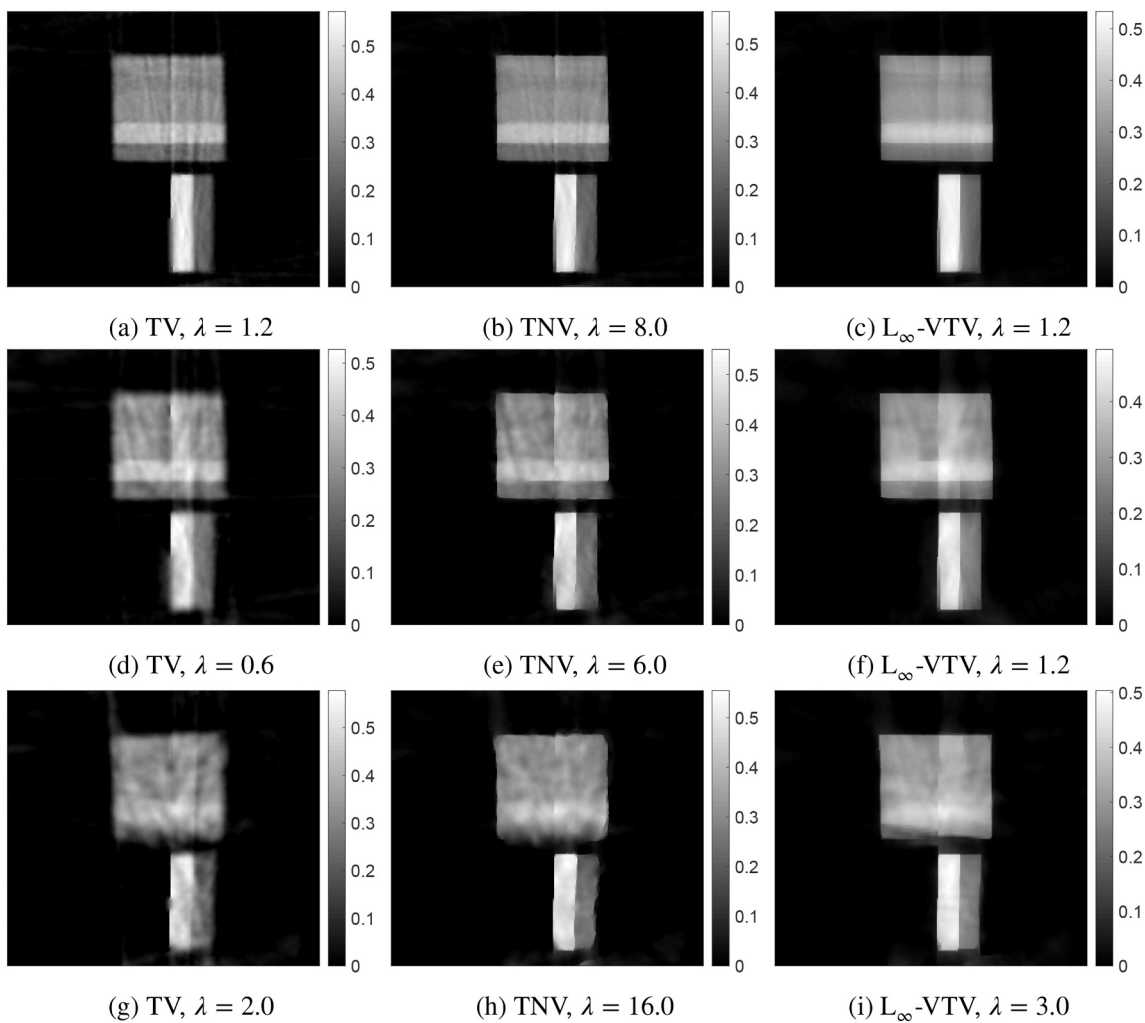


Fig. 6. Reconstructions from a decreasing number of projections. The reconstructions in the left, middle and right columns are respectively TV, TNV and L_{∞} -VTM, each corresponding to the optimal λ values presented in Fig. 5; (a)–(c) 36 projections; (d)–(f) 12 projections; (g)–(i) 7 projections. The gray scale bars represent the LACs (cm^{-1}) presented for 42 keV.

weighting parameter for the integration times of 50 ms, 10 ms and 2 ms. The maximal correlation coefficients for the TNV and L_{∞} -VTM

reconstructions become significantly larger than the coefficient for the TV reconstruction, as the integration time decreases. The λ value corresponding to the maximal correlation coefficient for each algorithm decreases as the integration time decreases, which indicates that the reconstruction requires more regularization to suppress higher noise, as expected.

Fig. 8 compares the TV, TNV and L_{∞} -VTM reconstructions for different integration times, each corresponding to the maximal correlation coefficient as the optimal reconstruction. In general, the TNV and L_{∞} -VTM joint reconstructions outperform the TV reconstruction when the data SNR in each energy bin is reduced. The case of 2 ms of the lowest integration time shows that the TV reconstruction significantly suffers from blurring and over-smoothing, whereas the joint reconstructions appear to be less noisy, sharper and better at preserving the edges. Thus, the joint reconstructions show better robustness to the measurements with lower photon counts compared to the bin-by-bin TV reconstruction. For 10 ms and 2 ms of the low-SNR cases, the L_{∞} -VTM with noticeably sharper edges and less structural artifacts in turn outperforms the TNV reconstruction.

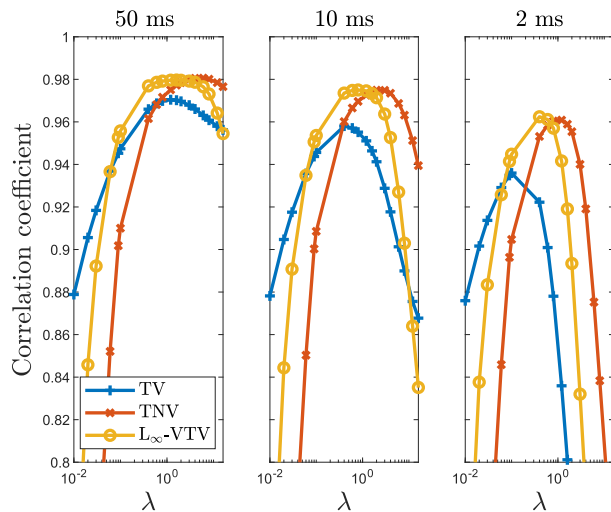


Fig. 7. Correlation coefficients as a function of weighting parameter λ for different detector integration times. Note the logarithmic scale in the x-axis.

5.4. Noise in certain energy bins

Significant noise in certain energy bins can be caused by metal objects in a sample. This can reduce the photon counts leading to photon

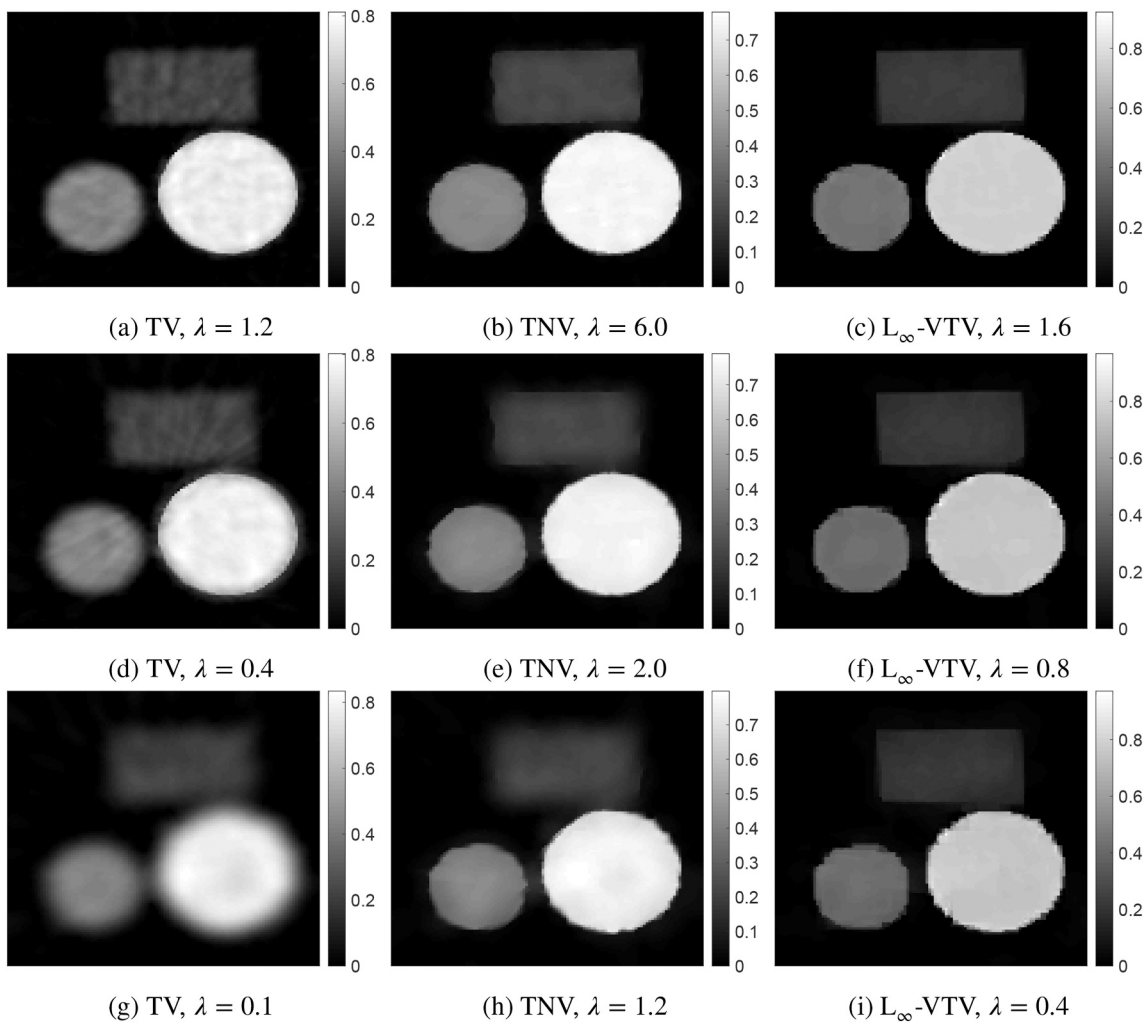


Fig. 8. Reconstructions from different detector integration times. The reconstructions in the left, middle and right columns are respectively TV, TNV and L_∞ -VTV, each corresponding to the optimal λ values presented in Fig. 7; (a)–(c) 50 ms; (d)–(f) 10 ms; (g)–(i) 2 ms. The gray scale bars represent the LACs (cm^{-1}) presented for 61.9 keV.

starvation and create metal artifacts in the reconstructions. Metal artifacts influence primarily the low energy bins and can be more severe resulting in less reliable material characterization. To estimate the robustness of the algorithms to such artifacts, we added Gaussian noise to sinogram data with a standard deviation (σ) of 0.5, 1.0 and 1.5. The noise was introduced to the two bins among the 15 energy bins used, that are 48.7 keV and 101.6 keV. These bins were specifically selected

such that they are far apart from each other, and one bin represents a high flux bin and the other a bin with low flux. Fig. 9 shows the correlation coefficients as a function of photon energy for each σ , obtained with each reconstruction algorithm. The correlation coefficients for each algorithm were reproduced based on the λ values that give the highest mean correlation coefficients for the case of $\sigma = 1.5$. Note that the mean correlation coefficient is calculated from the coefficients for each of 15

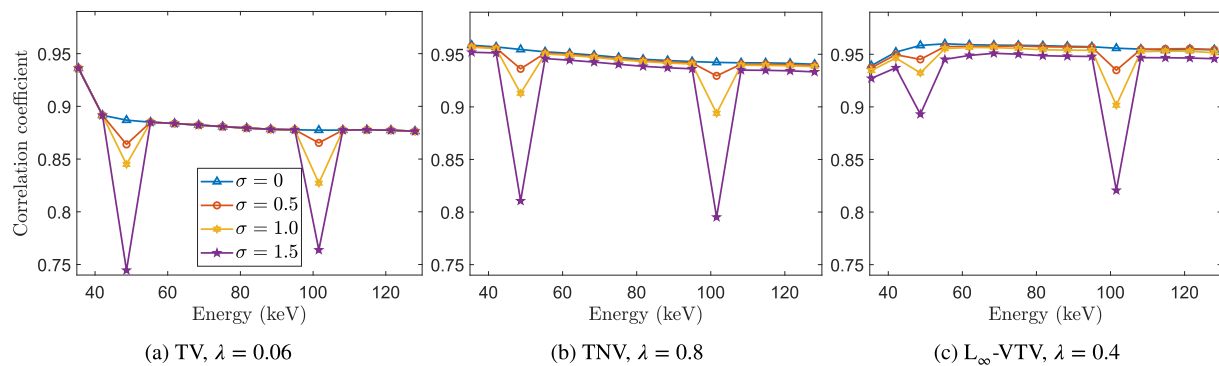


Fig. 9. Correlation coefficients as a function of photon energy, obtained from sinogram data in which high Gaussian noise with standard deviation (σ) of 0.5, 1.0 and 1.5 is added to certain energies of 48.7 keV and 101.6 keV.

energy bins used. The results presented in this subsection were obtained using the sample illustrated in Fig. 2b, which was scanned with the integration time of 100 ms and reconstructed from 12 projections. The total exposure time was the same as for the integration time per projection.

As can be noted from the plots, there are no interactions between energy bins for TV, as expected, whereas TNV and L_∞ -TV show correlations between energy bins and therefore have noticeably smaller drop-offs in the correlation coefficients for the affected bins. Thus, the joint reconstruction algorithms compensate for significantly high noise levels in certain energy bins by effectively using the unaffected bins, for which couplings between bins lead to some decreases in overall reconstruction quality. L_∞ -TV in turn outperforms TNV in compensating such increased noise, and significantly improves the reconstruction quality in the lower energy bins. This property of L_∞ -TV can be highly important to reduce metal artifacts that mainly affect lower energies.

5.5. The L-curve criterion

The L-curve is a plot that can show the trade-off between the regularization term and the respective data fidelity term defined in Eq. (4), as the weighting parameter λ changes [35]. The data fidelity term is the squared reprojection error, which is summed over all energy bins as $\|Au_\lambda - p\|_2$. The regularization term $\mathcal{R}_{TV}(u)$ for TV defined in Eq. (5) is computed independently for each energy bin, and summed over all energy bins for plotting the L-curve. The regularization terms for TNV ($\mathcal{R}_{TJV}(u)$) and L_∞ -TV ($\mathcal{R}_{L_\infty-TV}(u)$) are defined in Eq. (6) and Eq. (7), respectively, and are common to all energy bins. The L-curve graphical tool has the potential to show the optimal λ value for the regularized reconstruction without using the ground truth image, which is required for the correlation coefficient. The L-curve criterion is that the optimal λ values theoretically lie on the corner of the L-curve, while the values on the flat and vertical parts of the curve lead to an over- and under-regularized reconstruction, respectively. The L-curve is represented on a log-log scale for the Tikhonov regularization [35]. Yang et al. [36] showed that using a linear-linear representation of the L-curve gives a suitable L-shape for TV reconstruction. Similarly, we found that a linear-linear representation is more suitable for the algorithms explored in this work.

The results presented in this subsection were obtained using the sample illustrated in Fig. 2b, which was scanned with the integration time of 100 ms and reconstructed from only 12 projections. The total exposure time is equal to the integration time for each projection. Fig. 10 shows the correlation coefficients as a function of λ and the L-curve for each algorithm. The L_∞ -TV presents the most accurate match between the two λ values corresponding to the maximal correlation coefficient and to the corner of the curve, while the TV demonstrates the least accurate correspondence. The L-curve criterion for the TV results in an

over-regularized reconstruction yielding severe over-smoothing. One reason may be that the TV tends to be over-regularized when the reconstruction is performed from few projections or from data with low SNRs as presented in the Subsections 5.2 and 5.3. Hanke [37] previously reported a similar limitation of the L-curve criterion for the Tikhonov regularization that the smoother the reconstruction, the lower the accuracy of λ estimation.

5.6. Classification performance as a function of λ

The material classification performance is evaluated for each reconstruction algorithm based on the SIMCAD method described in the Section 4. The results presented in this subsection were obtained using the reference and test materials, which are tabulated in Table 2 and Table 3, respectively. For each projection, the total exposure time was 8 s, while the integration time was set to 100 ms. Fig. 11 presents the mean (for all materials estimated) percent relative deviations for ρ_e and Z_{eff} as a function of λ obtained with 12, 7 and 7 noisy projections. The case of 7 noisy projections means that Gaussian noise with standard deviation $\sigma = 0.05$ was artificially introduced into the experimental data after the spectral correction described in the Subsection 2.3. To test the robustness of each algorithm to noisy data for material classification, the noise was added to all the 15 energy bins and for all the reference and test materials listed in Table 2 and Table 3, which are used for the calibration step and (ρ_e, Z_{eff}) calculation, respectively. The relative deviations corresponding to the optimal λ values for each algorithm are presented in Table 5. The algorithms produce similar classification results in the case of 12 projections. The joint TNV and L_∞ -TV reconstructions clearly yield better classification performance than the bin-by-bin TV reconstruction in the cases of 7 and 7 noisy projections. The L_∞ -TV in turn has better classification performance than the TNV. The SIRT algorithm that is not presented in the plot showed significantly higher deviations of 8.4% for ρ_e and 2.4% for Z_{eff} for 12 projections, and 13.9% and 3.0% for 7 projections, respectively.

Fig. 12a shows the classification results for the different materials obtained from 7 projections. The L_∞ -TV gives the lowest deviations for both material features for POM-H plastic material that can be a common explosive simulant with similar chemical compositions [38]. Fig. 12b shows the relative deviations as a function of λ for the L_∞ -TV obtained from 7 projections, for the different materials. The L_∞ -TV thus reaches the optimal classification performance in the range of λ between 20 and 40. It is also noteworthy that we found in our implementation that the L_∞ -TV requires 10.6% and 52.3% shorter computation time for the material features estimation than the TNV and TV, respectively.

6. Conclusion

We have presented the L_∞ -TV joint reconstruction algorithm with

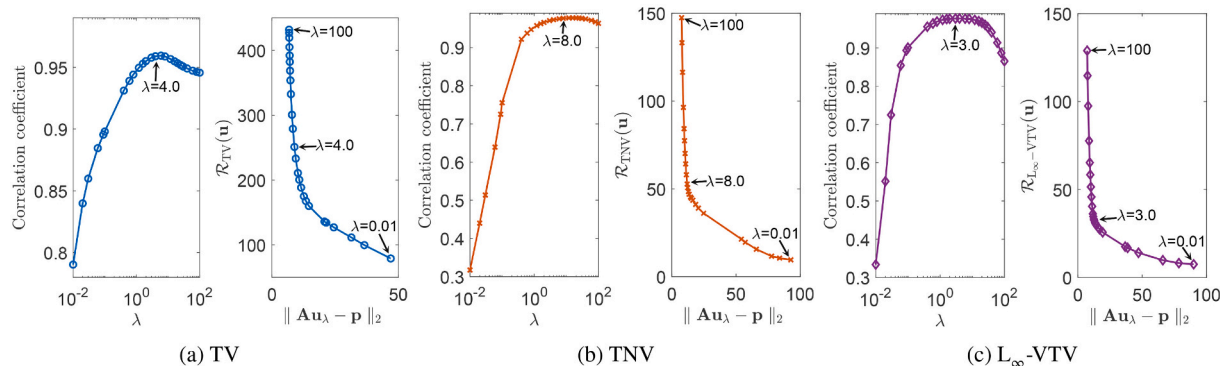


Fig. 10. Correlation coefficients as a function of weighting parameter λ and the L-curve for each reconstruction algorithm. Note the logarithmic scale in the x-axis for the correlation coefficient.

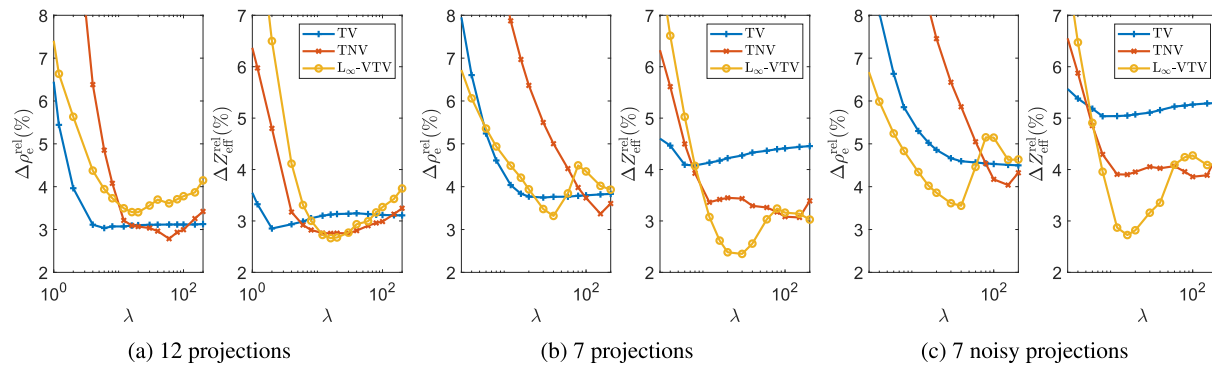


Fig. 11. The percent relative deviations for (ρ_e , Z_{eff}) as a function of weighting parameter λ , obtained with 12, 7 and 7 noisy projections. The mean relative deviations computed from the absolute values of relative deviations for each material listed in Table 3 are shown. Note the logarithmic scale in the x-axis.

Table 5

The estimation of the material's features for 12, 7 and 7 noisy projections, corresponding to the optimal λ values for each reconstruction algorithm. See Fig. 11 for the classification results from the whole range of λ .

Projections	TV			TNV			L_∞ -VTV		
	λ	$\Delta\rho_e^{\text{rel}}(\%)$	$\Delta Z_{\text{eff}}^{\text{rel}}(\%)$	λ	$\Delta\rho_e^{\text{rel}}(\%)$	$\Delta Z_{\text{eff}}^{\text{rel}}(\%)$	λ	$\Delta\rho_e^{\text{rel}}(\%)$	$\Delta Z_{\text{eff}}^{\text{rel}}(\%)$
12	6	3	3	60	2.8	2.9	16	3.4	2.7
7	16	3.8	4.2	150	3.4	3.1	30	3.5	2.4
7 noisy	30	4.7	5.1	150	4.0	3.9	20	3.9	2.8

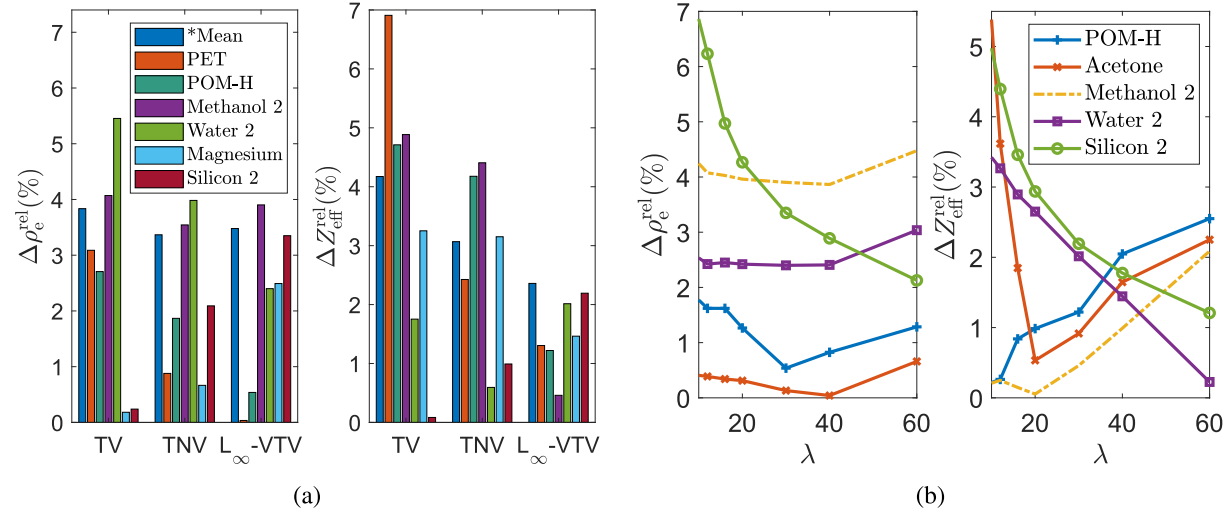


Fig. 12. Plots of material features estimation accuracy, obtained with 7 projections. (a) The percent relative deviations for (ρ_e , Z_{eff}) corresponding to the optimal λ for each reconstruction algorithm, as the results for the whole range of λ are shown in Fig. 11. The mean deviation was calculated from the absolute values of relative deviations for each material listed in Table 3. (b) The percent relative deviations for (ρ_e , Z_{eff}) as a function of λ for the L_∞ -VTV. The absolute values of relative deviations are shown.

focus on security screening applications, based on the real experimental data acquired with a laboratory X-ray spectral CT. We tested the L_∞ -VTV against another state-of-the-art joint reconstruction of TNV, and bin-by-bin TV and SIRT reconstructions. How each algorithm is implemented and the iteration number is fixed based on the correlation coefficient have been shown. The correlation coefficient is used to find how well the reconstruction image quality is correlated with the ground truth image. The reconstruction quality for each algorithm has been evaluated performing the reconstruction from few projections and low photon counts. We found that the joint reconstruction algorithms have significantly higher reconstruction performance compared to bin-by-bin reconstructions. The L_∞ -VTV in turn has better reconstruction quality than the TNV. We tested the robustness of each algorithm to significantly high noise introduced into specific energy bins. The L_∞ -VTV appears to

effectively alleviate such noise using information from unaffected bins, and thereby achieve better reconstruction for all the energy bins. Thus, the L_∞ -VTV correlates the image gradients strongly over different energy bins, resisting outliers in gradient magnitudes. This property can be very useful for handling metal artifacts, which mainly affect the low-energy bins. Furthermore, we studied the L-curve for each reconstruction algorithm, which may show the potential to find the optimal weighting parameter, and relies on the reconstructed sample itself without the ground truth image. The L_∞ -VTV shows the most accurate correspondence between the two optimal weighting parameters obtained with the correlation coefficient and the L-curve criterion. Lastly, we compared the material classification performances of the algorithms for few and noisy projections, based on the classification method that estimates the pair of material features (ρ_e , Z_{eff}) from spectral CT. The

broad range of materials have been used for the classifications. The joint reconstruction algorithms appear to have significantly better classification performances compared to the bin-by-bin reconstructions, while the L_∞ -VTV in turn has better classification accuracy and requires shorter computation time than the TNV. The algorithms presented could easily be adapted for 3D CT setups.

Data and code availability

The raw and corrected data required to obtain the presented results are available to download from [39]. The implementations of our codes for L_∞ -VTV and TNV joint reconstruction algorithms are available at <https://github.com/JuliaTomo/XfromProjections.jl>.

CRediT authorship contribution statement

Doniyor Jumanazarov: Conceptualization, Methodology, Software, Formal analysis, Investigation, Data curation, Writing – original draft, Visualization. **Jakeoung Koo:** Methodology, Software, Validation, Formal analysis, Writing – original draft. **Jan Kehres:** Resources, Writing – review & editing. **Henning F. Poulsen:** Writing – review & editing, Supervision. **Ulrik L. Olsen:** Validation, Resources, Data curation, Writing – review & editing, Supervision. **Mihai Iovea:** Validation, Writing – review & editing, Supervision, Funding acquisition.

Declaration of Competing Interest

The authors declare that they have no known competing financial interests or personal relationships that could have appeared to influence the work reported in this paper.

Acknowledgements

This project has received funding from the European Union Horizon 2020 research and innovation programme under the Marie Skłodowska-Curie grant agreement No. 765604 as part of the MULTISCALE, Multimodal and Multidimensional imaging for EngineeRING project (MUMMERING Innovative Training Network, www.mummering.eu) and from the EIC FTI program (project 853720).

The authors want to acknowledge also the 3D Imaging Center at DTU, where the experiments have been conducted.

References

- [1] L.I. Rudin, S. Osher, E. Fatemi, Nonlinear total variation based noise removal algorithms, *Physica D* 60 (1992) 259–268.
- [2] J. Song, Q.H. Liu, G.A. Johnson, C.T. Badea, Sparseness prior based iterative image reconstruction for retrospectively gated cardiac micro-CT, *Med. Phys.* 34 (2007) 4476–4483.
- [3] J. Bian, J. Wang, X. Han, E.Y. Sidky, L. Shao, X. Pan, Optimization-based image reconstruction from sparse-view data in offset-detector CBCT, *Phys. Med. Biol.* 58 (2013) 205–230.
- [4] E.Y. Sidky, C.M. Kao, X. Pan, Accurate image reconstruction from few-views and limited-angle data in divergent-beam CT, *J. X-Ray Sci. Technol.* 14 (2006) 119–139.
- [5] S.G. Azevedo, H.E. Martz, M.B. Aufderheide, W.D. Brown, K.M. Champliey, J. S. Kallman, G.P. Roberson, D. Schneberk, I.M. Seetho, J.A. Smith, System-independent characterization of materials using dual-energy computed tomography, *IEEE Trans. Nucl. Sci.* 63 (2016) 341–350.
- [6] R. Garnett, A comprehensive review of dual-energy and multi-spectral computed tomography, *Clin. Imaging* 67 (2020) 160–169.
- [7] M. Busi, K.A. Mohan, A.A. Dooraghi, K.M. Champliey, H.E. Martz, U.L. Olsen, Method for system-independent material characterization from spectral X-ray CT, *NDT & E Int.* 107 (2019) 102136.
- [8] S. Devadithya, D. Castañón, Enhanced material estimation with multi-spectral ct, *Electron Imaging* 2021 (2021), 229–1.
- [9] M. Busi, U.L. Olsen, E.B. Knudsen, J.R. Frisvad, J. Kehres, E.S. Dreier, M. Khalil, K. Haldrup, Simulation tools for scattering corrections in spectrally resolved x-ray computed tomography using mxctrace, *Opt. Eng.* 57 (2018), 037105.
- [10] P. Blomgren, T.F. Chan, Color TV: Total variation methods for restoration of vector-valued images, *IEEE Trans. Image Process.* 7 (1998) 304–309.
- [11] K.M. Holt, Total nuclear variation and Jacobian extensions of total variation for vector fields, *IEEE Trans. Image Process.* 23 (2014) 3975–3989.
- [12] B. Recht, M. Fazel, P.A. Parrilo, Guaranteed minimum-rank solutions of linear matrix equations via nuclear norm minimization, *SIAM Rev.* 52 (2010) 471–501.
- [13] D.S. Rigie, P.J. La Rivière, Joint reconstruction of multi-channel, spectral CT data via constrained total nuclear variation minimization, *Phys. Med. Biol.* 60 (2015) 1741–1762.
- [14] D.S. Rigie, A.A. Sanchez, P.J. La Rivière, Assessment of vectorial total variation penalties on realistic dual-energy CT data, *Phys. Med. Biol.* 62 (2017) 3284–3298.
- [15] Z. Zhong, W.J. Palenstijn, J. Adler, K.J. Batenburg, EDS tomographic reconstruction regularized by total nuclear variation joined with HAADF-STEM tomography, *Ultramicroscopy* 191 (2018) 34–43.
- [16] J. Gregor, T. Benson, Computational analysis and improvement of SIRT, *IEEE Trans. Med. Imaging* 27 (2008) 918–924.
- [17] T. Miyata, Y. Sakai, Vectorized total variation defined by weighted L infinity norm for utilizing inter channel dependency, in: *Proceedings - International Conference on Image Processing, ICIP, 2012*, pp. 3057–3060.
- [18] J. Duran, M. Moeller, C. Sbert, D. Cremers, On the Implementation of Collaborative TV Regularization: Application to Cartoon+Texture Decomposition, *Image Processing On Line* 5, 2016, pp. 27–74.
- [19] D. Jumanazarov, J. Koo, M. Busi, H.F. Poulsen, U.L. Olsen, M. Iovea, System-independent material classification through X-ray attenuation decomposition from spectral X-ray CT, *NDT & E Int.* 116 (2020) 102336.
- [20] R.E. Alvarez, A. Macovski, Energy-selective reconstructions in X-ray computerised tomography, *Phys. Med. Biol.* 21 (1976) 733–744.
- [21] L. Salvo, M. Suéry, A. Marmottant, N. Limodin, D. Bernard, 3D imaging in material science: application of X-ray tomography, *Compt. Rend. Phys.* 11 (2010) 641–649.
- [22] E. Maire, P.J. Withers, Quantitative X-ray tomography, *Int. Mater. Rev.* 59 (2014) 1–43.
- [23] A.H. Compton, S.K. Allison, et al., *X-Rays in Theory and Experiment*, Van Nostrand, New York, NY, USA, 1935.
- [24] W.V. Mayneord, The significance of the roentgen, in: *Acta of the International Union Against Cancer* 2, 1937, p. 271.
- [25] F.W. SPIERS, Effective atomic number and energy absorption in tissues, *Br. J. Radiol.* 19 (1946) 52–63.
- [26] Matteo Busi, Enhanced Security Screening Using Spectral X-ray Imaging, Phd thesis, Technical University of Denmark, 2019.
- [27] A. Brambilla, P. Ouvrier-Buffet, J. Rinkel, G. Gonon, C. Boudou, L. Verger, CdTe linear pixel X-ray detector with enhanced spectrometric performance for high flux X-ray imaging, *IEEE Trans. Nucl. Sci.* 59 (2012) 1552–1558.
- [28] M. Ellenbogen, R. Bijjani, Liquids and homemade explosive detection, in: *Optics and Photonics in Global Homeland Security V and Biometric Technology for Human Identification VI* vol. 7306, International Society for Optics and Photonics, 2009, <https://doi.org/10.1117/12.821806>, p. 73060Y.
- [29] S. Kim, J. Chen, T. Cheng, A. Gindulyte, J. He, S. He, Q. Li, B.A. Shoemaker, P. A. Thiessen, B. Yu, L. Zaslavsky, J. Zhang, E.E. Bolton, PubChem 2019 Update: Improved Access to Chemical Data, 2019. URL.
- [30] E.S. Dreier, J. Kehres, M. Khalil, M. Busi, Y. Gu, R. Feidenhans, U.L. Olsen, Spectral correction algorithm for multispectral CdTe x-ray detectors, *Opt. Eng.* 57 (2018) 16.
- [31] A. Chambolle, T. Pock, A first-order primal-dual algorithm for convex problems with applications to imaging, *J. Math. Imaging Vis.* 40 (2011).
- [32] H.H. Bauschke, P.L. Combettes, *Convex Analysis and Monotone Operator Theory in Hilbert Spaces*, CMS Books in Mathematics, Springer International Publishing, Cham, 2017, <https://doi.org/10.1007/978-3-319-48311-5>.
- [33] L.N. Trefethen, D. Bau, *Numerical Linear Algebra*, Society for Industrial and Applied Mathematics, Philadelphia, 1997.
- [34] J. Nocedal, S.J. Wright, *Numerical Optimization*, Springer, New York, 1999.
- [35] P.C. Hansen, The L-curve and its use in the numerical treatment of inverse problems, in: P. Johnston (Ed.), *Computational Inverse Problems in Electrocardiology* 4, 2000, pp. 119–142. Advances in Computational Bioengineering.
- [36] X. Yang, R. Hofmann, R. Dapp, T. van de Kamp, T.D.S. Rolo, X. Xiao, J. Moosmann, J. Kashef, R. Stotzka, TV-based conjugate gradient method and discrete L-curve for few-view CT reconstruction of X-ray *in vivo* data, *Opt. Express* 23 (2015) 5368.
- [37] M. Hanke, Limitations of the L-curve method in ill-posed problems, *BIT Numer. Math.* 36 (1996) 287–301.
- [38] J. Rinkel, G. Beldjoudi, V. Rebuffel, C. Boudou, P. Ouvrier-buffet, G. Gonon, L. Verger, A. Brambilla, Experimental evaluation of material identification methods with CdTe X-ray spectrometric detector, *IEEE Trans. Nucl. Sci.* 58 (2011) 2371–2377.
- [39] D. Jumanazarov, J. Koo, J. Kehres, H.F. Poulsen, U.L. Olsen, M. IOVEA, Material classification from sparse spectral X-ray CT using vectorial total variation based on L infinity norm [Data set], Zenodo (2021), <https://doi.org/10.5281/zenodo.4780625>.



Doniyor Jumanazarov is a PhD fellow at the Department of Physics at Denmark Technical University (DTU), Kongens Lyngby, Denmark. He obtained his BS degree in physics from the National University of Uzbekistan, Tashkent, Uzbekistan, and his MS degree in Molecular Photonics for bio- and nanotechnologies (MONABIPHOT) from the École Normale Supérieure de Cachan, Cachan, France, in 2012 and 2018, respectively.



Henning F. Poulsen is employed at DTU Physics since 2012. Henning pioneered several x-ray microscopy methods enabling multiscale mapping of materials properties from the macroscopic and down to nanometre length scales. He heads the 3D Imaging Centre at DTU and is Principal Investigator on a number of European and national projects with the aim of introducing X-ray methods to industry.



Jakeoung Koo received his B.Sc. and M.Sc. in Computer Science from Chung-Ang University, South Korea in 2015 and 2017, respectively. He is now a Ph.D. student in Technical University of Denmark (DTU), Kongens Lyngby, Denmark. His research interests lie in Computed Tomography and Computer Vision.



Ulrik L. Olsen is a senior research engineer at DTU Physics since 2013. He obtained his Ph.D. degree in 2009 from Copenhagen University. He is an expert in X-ray instrumentation and specialises in spectral X-ray detectors, data acquisition and processing. Ulrik's current research interest is the use of spectral detectors for security applications for improved reconstruction and material identification.



Jan Kehres is a research engineer at DTU Physics. He received his PhD in operando investigation of catalyst nanoparticles using X-ray scattering and continued in this field of research as a postdoctoral researcher. His current field of research is the application of energy-dispersive detector technology for X-ray scattering and advanced imaging modalities with a focus on material identification of illicit materials for security applications. Jan has an extended background in developing instruments in the field of X-Ray science.



Mihai Iovea, Engineer in Physics, Senior Research Scientist, Ph.D in Physics. He has over 30 years' experience in X-Ray Imaging projects research & development for Security and Non-Destructive Testing. Interested in X-ray 2D&3D Tomography and Digital Radiography techniques, such as: dual/multi energy, diffraction, back-scattering applied in for threats detection, high-resolution in-line X-ray scanners for fast industrial non-destructive testing.